

Reversing Néel Vector in \mathcal{PT} -Antiferromagnets by Nonreciprocal Light Scattering

Qianqian Xue¹ and Jian Zhou^{1,*}

¹Center for Alloy Innovation and Design, State Key Laboratory for Mechanical Behavior of Materials, Xi'an Jiaotong University, Xi'an, 710049, China

Antiferromagnetic (AFM) spintronics has been receiving tremendous attention due to their ultrafast kinetics, zero stray field, immune to external magnetic field, and potential to minimizing magnetic storage devices. The optical control of AFM Néel vector has become a hectic topic during recent years, which could facilitate the AFM utilization in practical systems. In this work, we propose a nonreciprocal light scattering mechanism to flip the Néel vector in parity-time (\mathcal{PT}) combined AFM multilayers, by estimating the energy contrast between the bistable Néel polarization configurations. We illustrate our theory using a low energy $\mathbf{k} \cdot \mathbf{p}$ model, and perform *ab initio* calculations on two typical *A*-type AFM materials, MnBi₂Te₄ and CrI₃ thin films. We show that varying incident photon frequency could modulate the relative stability between the bistable Néel vector state, which also depends on the light handedness. According to this theory, our parameter-independent calculations on the Néel vector diagram shows consistent predictive results with recent experimental observations. This mechanism provides an effective route to controlling the AFM order parameter through photo-magnetic interaction.

Introduction. Manipulating different orders of parameter is one of the most essential aspects in condensed matter physics and materials science, leading to various pivotal practical applications. In addition to many ferroic (such as ferroelectric, ferromagnetic, and ferroelastic) orders that have been widely-used, recent years have witnessed increasing interests and extensive attention in antiferro-systems [1–6]. For instance, antiferromagnetic (AFM) materials that possess zero intrinsic net magnetic moments have been demonstrated to exhibit ultrafast kinetics and high resolution spintronic processes, described by its order parameter such as the Néel vector \mathcal{N}_0 in collinear AFMs. The Néel vector direction determines the magnetic symmetry of the system (with spin-orbit coupling, SOC), hence it could precisely control and tune various transport and optical responses, such as anomalous Hall effect [7–10], nonlinear Hall effect [11–14], bulk photovoltaic effect [15–20], and valley polarization [21, 22].

For practical applications of AFMs, a natural question is how to control and manipulate \mathcal{N}_0 [23–27]. As with vanishing magnetic moments, an magnetic field in general cannot change its direction and other recipes need exploration. Among them, optical approaches are very attractive as light is contactless and does not introduce unwanted impurities and disorders into the sample. The ultrafast nature also guarantees efficient control with high resolution. While many works focus on the light-induced magnetization reorientation and demagnetization in ferromagnets [28–31], it still remains an open question on how to understand the fundamental mechanism of light-induced \mathcal{N}_0 flip in compensated AFMs. Here, we focus on *A*-type AFM multilayers with \mathcal{PT} (combined parity and time-reversal) symmetry, which usually show a bistable configuration with degenerate $-\mathcal{N}_0$ and \mathcal{N}_0 , such as even layered MnBi₂Te₄ [32–34] and CrI₃ [35, 36] films. Both these materials have been experimentally demonstrated

to exhibit an out-of-plane easy axis, and prefer intralayer ferromagnetic and interlayer AFM configuration (the former one shows an axion insulating feature). We propose a symmetry-adapted microscopic mechanism that incorporates nonreciprocal light scattering process as it normally irradiates on the multilayers. Accordingly, we derive a light-induced free energy variation formalism, to show how nonreciprocally propagating circularly polarized light (CPL) breaks \mathcal{P} and \mathcal{T} symmetries simultaneously. Hence, CPL lifts the energy degeneracy between \mathcal{N}_0 and $-\mathcal{N}_0$ states. We then adopt a simplified $\mathbf{k} \cdot \mathbf{p}$ model to illustrate this process, and perform first-principles density functional theory (DFT) to apply such a theory in both MnBi₂Te₄ and CrI₃ bilayers. We suggest that depending on the CPL handedness ($\sigma\pm$) and light frequency (or wavelength), the relative stability between \mathcal{N}_0 and $-\mathcal{N}_0$ can be switched. Our parameter-free DFT calculation predictions on the wavelength-dependent relationship between $\sigma\pm$ and $\pm\mathcal{N}_0$ give consistent results with recent experimental measurements, validating our theoretical mechanism.

In the bistable *A*-type AFMs with parity-time \mathcal{PT} symmetry, the \mathcal{N}_0 configuration is degenerate with $-\mathcal{N}_0$, protected by \mathcal{P} and \mathcal{T} [Fig. 1(a)]. Hence, in order to lift their degeneracy and trigger Néel vector reversal, one has to simultaneously break both these two symmetries. We will focus on CPL irradiation here as it naturally breaks \mathcal{T} . When the sample thickness is on the order of a few to a few tens of nanometers (well-below light penetration depth) and laser pulses (rather than continuous wave) are assumed, the thermal effect can be safely eliminated. Hence, we will only consider athermic photomagnetic process [37].

Theory on light-induced free energy variation. We consider normal incident light onto bistable AFM multilayers [Fig. 1(b)]. The alternating magnetic field component of light is omitted as it is orders of magnitude smaller

than the electric field components. Hence, the light is described by $\vec{\mathcal{E}}_\omega(t) = \text{Re}\vec{E}e^{i\omega t}$. The in-plane electric field magnitude vector is $\vec{E} = E_\omega(1, \eta, 0)$ with $\eta = \pm i$ indicating the right-handed $\sigma+$ and left-handed $\sigma-$ light. We use $\vec{e}^{\sigma\pm} = (1, \eta, 0)$ to denote the electric field unit vector. Since the unit cell size is much smaller than the laser spot, the lateral inhomogeneity can be safely omitted ($\mathbf{q} = 0$ interaction). Here, we assume that the energy transfer between light electric field and the sample stems from two aspects. Firstly, when the photon energy $\hbar\omega$ is above the sample bandgap E_g , light absorption naturally exists by exciting electron-hole pairs, and the internal energy gains. This is scaled by light absorbance. For ultrathin materials with thickness of d , the absorbance is

$$A_{\mathcal{N}_0}^{\sigma\pm}(\omega) = \frac{d}{c\varepsilon_0} \vec{e}^{\sigma\pm,*} \cdot \vec{\sigma}'_{\mathcal{N}_0}(\omega) \cdot \vec{e}^{\sigma\pm}, \quad (1)$$

where c denotes the speed of light in vacuum and ε_0 is vacuum permittivity. Here, $\vec{\sigma}'(\omega)$ refers to frequency-dependent optical conductivity, which relates to the susceptibility function by $\chi_{ij}(\omega) = \frac{i}{\varepsilon_0\omega} \sigma_{ij}(\omega)$. Eq. (1) is valid when d is much smaller than photon wavelength, measuring energy gain per area. Then the total free energy per area raises according to $\mathcal{G}_{\text{abs},\mathcal{N}_0}^{\sigma\pm}(\omega) = nA\hbar\omega$ with n describing expectation number of photons that irradiate on the sample per area.

On the other hand, we would like to introduce another mechanism that also affects the potential energy landscape. This is in analogous to the optical tweezer technique [38] and has been largely overlooked previously. To the lowest order, it describes light scattering with respect to elementary excitations. Thermodynamically, the light scattering effect adds an additional potential energy (per area) in the form of [39, 40]

$$\mathcal{G}_{\text{sc},\mathcal{N}_0}^{\sigma\pm}(\omega) = d \left[\vec{e}^{\sigma\pm,*} \cdot \frac{\vec{\sigma}''_{\mathcal{N}_0}(\omega)}{4\omega} \cdot \vec{e}^{\sigma\pm} \right] E_\omega^2. \quad (2)$$

Very recently, this light scattering effect has been used to predict nonvolatile phase transition in nonmagnetic materials under nonresonant light irradiation, and its validity has been quantitatively demonstrated via recent experiments [41, 42]. In magnetic materials, broken of \mathcal{T} yields finite nondiagonal components in $\vec{\sigma}$. Recently, Eq. (2) is also derived according to nonequilibrium steady state theory of a fast oscillating system on a slow varying field, termed as ‘‘ponderomotive’’ potential [43]. Hence, it belongs to Floquet engineering picture. According to Eq. (2), $\mathcal{G}_{\text{sc}}(\omega)$ scales with E_ω^2 (or light intensity I), hence it lies on the same order with $\mathcal{G}_{\text{abs}}(\omega)$. In a simple damped harmonic model, one sees $\mathcal{G}_{\text{sc}} \propto \text{Re}[1/(\omega^2 - \omega_0^2 + i\gamma\omega)]$. Thus, it could occur when photon energy is above and below E_g . As a scattering process, it keeps the photon number n to be unchanged.

Our light-induced Néel vector flipping mechanism is established upon the above two mechanisms. When the

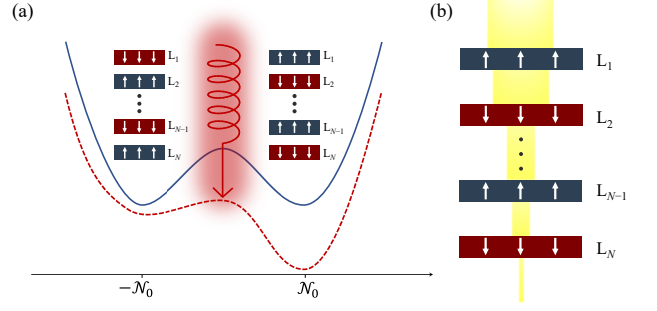


FIG. 1. Schematic plot of circularly polarized light induced Néel flip. (a) Modulation of energy profile under light, with $\pm\mathcal{N}_0$ representing bistable states. (b) Light attenuation across layers. The scattering and attenuation break time-reversal \mathcal{T} and inversion symmetry \mathcal{P} , respectively, and their synergistic effect could flip the Néel vector.

CPL irradiates onto the multilayer, light attenuation occurs as each van der Waals (vdW) layer absorbs the photon flux [Fig. 1(b)]. This corresponds to a nonreciprocal process that breaks \mathcal{P} . In particular, when the normal incident CPL irradiates onto the multilayer (with a total N vdW layers) along $-z$, at the i^{th} vdW layer, its free energy per area varies according to

$$\begin{aligned} \mathcal{G}_{\mathcal{N}_0}^{\sigma\pm}(L_i, \omega) &= \mathcal{G}_{0,\mathcal{N}_0}(L_i) + \mathcal{G}_{\text{sc},\mathcal{N}_0}^{\sigma\pm}(L_i, \omega) + \mathcal{G}_{\text{abs},\mathcal{N}_0}^{\sigma\pm}(L_i, \omega) \\ &= \mathcal{G}_{0,\mathcal{N}_0}(L_i) + d\lambda_{\mathcal{N}_0}^{\sigma\pm}(L_i, \omega) \left[\vec{e}^{\sigma\pm,*} \cdot \frac{\vec{\sigma}''_{\mathcal{N}_0}(L_i, \omega)}{4\omega} \cdot \vec{e}^{\sigma\pm} \right] E_\omega^2 \\ &\quad + \frac{d}{c\varepsilon_0} \vec{e}^{\sigma\pm,*} \cdot \vec{\sigma}'_{\mathcal{N}_0}(L_i, \omega) \cdot \vec{e}^{\sigma\pm} n_i \hbar\omega. \end{aligned} \quad (3)$$

Here, $\mathcal{G}_{0,\mathcal{N}_0}(L_i)$ denotes the free energy before CPL is irradiated. As the conductance and susceptibility tensor is scaled by $1/d$ (see below) in practical calculations, the specific choice of d value does not change the results for total energy variation. For A -type AFM multilayers, it is natural that $\sum_{i=1}^N \mathcal{G}_{0,\mathcal{N}_0}(L_i) = \sum_{i=1}^N \mathcal{G}_{0,-\mathcal{N}_0}(L_i)$, with N being an even number denoting the total layer numbers. As light is attenuated, n_i monotonously reduces from n_0 (total photon number per area in vacuum within the pulse) under above E_g light illumination. Here, we introduce an attenuation factor $\lambda_{\mathcal{N}_0}^{\sigma\pm}(L_i, \omega) = n_i/n_0 = \prod_{j=1}^{i-1} [1 - A_{\mathcal{N}_0}^{\sigma\pm}(L_j, \omega)]$ that accounts for photon number elimination. We use the electromagnetic wave expectation energy flux to replace photon energy, and one has $n_i \hbar\omega = c\varepsilon_0 \lambda_{\mathcal{N}_0}^{\sigma\pm}(L_i, \omega) \tau E_\omega^2$, with τ being the light duration time (usually within one picosecond in a few pulses, taken to be 0.1 ps in our study). In this regard, the total energy per unit area profile is renormalized according to

$$\mathcal{G}_{\mathcal{N}_0}^{\sigma\pm}(\omega) = \sum_{i=1}^N \left[\mathcal{G}_{0,\mathcal{N}_0}(L_i) + (\vec{e}^{\sigma\pm,*} \cdot \vec{K} \cdot \vec{e}^{\sigma\pm}) E_\omega^2 \right], \quad (4)$$

in which we have

$$\begin{aligned} \overleftrightarrow{K}_{\mathcal{N}_0}(\mathbf{L}_i, \omega) &= \lambda^{\sigma\pm} d \left(\frac{\overleftrightarrow{\sigma}''}{4\omega} + \tau \overleftrightarrow{\sigma}' \right) \\ &= \varepsilon_0 \lambda^{\sigma\pm} d \left(-\frac{1}{4} \overleftrightarrow{\chi}' + \tau \omega \overleftrightarrow{\chi}'' \right). \end{aligned} \quad (5)$$

In this equation, both optical conductance $\overleftrightarrow{\sigma}$ and susceptibility $\overleftrightarrow{\chi}$ depend on layer index \mathbf{L}_i , Néel vector \mathcal{N}_0 , and incident frequency ω , which are omitted for clarity reason. Therefore, we can estimate the energy difference between \mathcal{N}_0 and $-\mathcal{N}_0$ states according to $\Delta\mathcal{G}^{\sigma\pm} = \mathcal{G}_{-\mathcal{N}_0}^{\sigma\pm}(\omega) - \mathcal{G}_{\mathcal{N}_0}^{\sigma\pm}(\omega) = \overleftrightarrow{e}^{\sigma\pm,*} \cdot [\sum_{i=1}^N \overleftrightarrow{K}_{-\mathcal{N}_0}(\mathbf{L}_i, \omega) - \overleftrightarrow{K}_{\mathcal{N}_0}(\mathbf{L}_i, \omega)] \cdot \overleftrightarrow{e}^{\sigma\pm} E_\omega^2$, which scales with the incident light intensity. Its sign depends on the incident photon energy $\hbar\omega$. Note that the above expression is not limited in vdW multilayers, and we give a continuum model for thin films in Supplemental Material [44–53].

Low energy model calculation.— We illustrate the above theory using a minimum $\mathbf{k} \cdot \mathbf{p}$ model [54, 55]

$$\begin{aligned} H(\mathbf{k}) &= \sum_{i,j=1}^N \{ (-1)^i [\hbar v_D (\hat{\mathbf{z}} \times \boldsymbol{\sigma}) \cdot \mathbf{k} + m_i^z \sigma_z] \delta_{ij} \\ &\quad + \Delta(\delta_{j,i+1} + \delta_{j,i-1})/2 \} c_{\mathbf{k},i}^\dagger c_{\mathbf{k},j}. \end{aligned} \quad (6)$$

Here, i (and j) denotes vdW layer index in the system, and $\boldsymbol{\sigma}$ is the Pauli matrix for spin degree of freedom. v_D is effective velocity at the Fermi energy, Δ denotes the vdW interactions between adjacent layers, and $m_i^z = -m_{i\pm 1}^z$ is the alternative z -component magnetization of each layer.

We take a structure with six layers in this model, and the parameters are taken as $\Delta = 0.5v_D$ and $m_z = \pm 2v_D$ (for \mathcal{N}_0 and $-\mathcal{N}_0$ states). Their parameter dependent results are summarized in Figs. S1 and S2 [44], suggesting that it is the m_z largely controls the optical susceptibility. We then calculate their susceptibility function $\chi^{\sigma\pm}(\omega)$ components. According to the independent particle approximation [56], the layer-resolved susceptibility is

$$\begin{aligned} \chi_{\alpha\beta}(\mathbf{L}_j, \omega) &= -\frac{e^2 L_c}{\varepsilon_0 N d} \int \frac{d^3 \mathbf{k}}{(2\pi)^3} \sum_{n,m} (f_{n\mathbf{k}} - f_{m\mathbf{k}}) \\ &\quad \times \frac{\langle u_{n\mathbf{k}} | \nabla_{k_\alpha} \hat{P}_j | u_{m\mathbf{k}} \rangle \langle u_{m\mathbf{k}} | \nabla_{k_\beta} | u_{n\mathbf{k}} \rangle}{\hbar(\omega_{n\mathbf{k}} - \omega_{m\mathbf{k}} - \omega - i/\tau_{el})}. \end{aligned} \quad (7)$$

Here, $|u_{n\mathbf{k}}\rangle$, $\hbar\omega_{n\mathbf{k}}$, and $f_{n\mathbf{k}}$ represent the Bloch wavefunction, eigenenergy, and Fermi-Dirac occupation of state n at \mathbf{k} , respectively. τ_{el} denotes the electron scattering lifetime. Note that it actually depends on the specific band index and momentum in each Bloch state, but its exact evaluation is computationally demanding and not straightforward even in a perfect crystal. The disorder and impurities are also phenomenologically incorporated

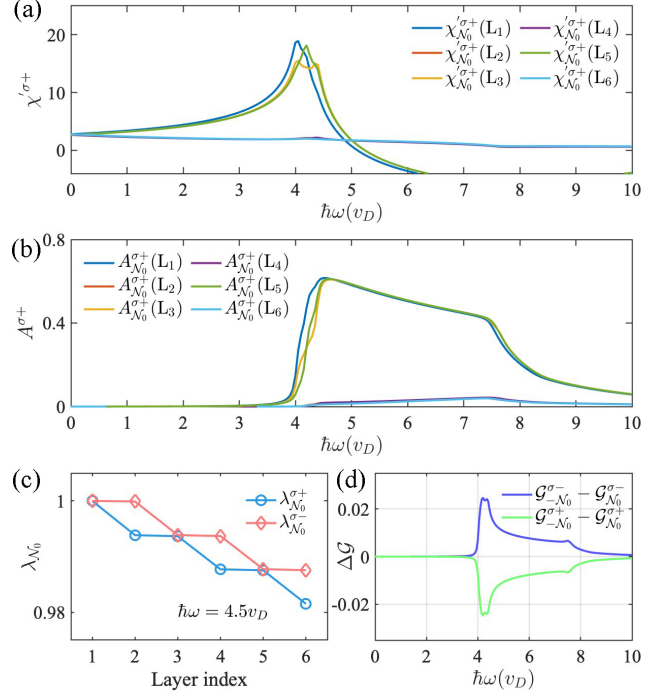


FIG. 2. Low energy model results. Layer index dependent (a) real part and (b) absorbance spectrum of susceptibility function under right-handed CPL for a six layered system, in \mathcal{N}_0 state. The odd (even) index represents spin up (down) layer. (c) Attenuation factor λ in the multilayer under left-handed and right-handed CPL. (d) Free energy difference between \mathcal{N}_0 and $-\mathcal{N}_0$ states, in arbitrary unit system.

into τ_{el} . Hence, we follow the conventional method and take a universal value in our discussion. We also note that its exact value does not affect the main results in this work. $\hat{P}_j = \sum_{l \in L_j} |u_l\rangle \langle u_l|$ denotes the projector operator on layer- j .

The results are plotted in Fig. 2. The real and imaginary parts of frequency dependent susceptibility in the whole system (summed over all six layers) satisfy the well-known Kramers-Kronig relation. The integral is performed in the 3D first Brillouin zone (BZ), and we introduce a scaling factor $\frac{L_c}{Nd}$ to eliminate the vacuum space contribution (L_c is supercell lattice constant along z) [39]. From Figs. 2(a) and 2(b), it is clearly seen that the $\sigma+$ light interacts with the spin up vdW layers stronger than the spin down layers in both $\chi'(\omega)$ and $A(\omega)$, thus presenting an even-odd oscillation behavior. Under an inversion operation \mathcal{P} , one can find that the layer-resolved optical response function satisfies $\chi_{\mathcal{N}_0}^{\sigma+}(\mathbf{L}_i, \omega) = \chi_{-\mathcal{N}_0}^{\sigma+}(\mathbf{L}_{N+1-i}, \omega)$ and $A_{\mathcal{N}_0}^{\sigma+}(\mathbf{L}_i, \omega) = A_{-\mathcal{N}_0}^{\sigma+}(\mathbf{L}_{N+1-i}, \omega)$. Similarly, applying \mathcal{T} one could yield $\sigma-$ illuminated results, $\chi_{\mathcal{N}_0}^{\sigma-}(\mathbf{L}_i, \omega) = \chi_{-\mathcal{N}_0}^{\sigma-}(\mathbf{L}_i, \omega)$ and $A_{\mathcal{N}_0}^{\sigma-}(\mathbf{L}_i, \omega) = A_{-\mathcal{N}_0}^{\sigma-}(\mathbf{L}_i, \omega)$. Our numerical results confirm these relationships. In Fig. 2(c), we plot the layer dependent attenuation factor $\lambda^{\sigma\pm}(\mathbf{L}_i)$ at a typi-

cal frequency $\omega = 4.5v_D$, slightly above the bandgap $E_g = 4.0v_D$. One sees a step-wise monotonously reduction trend, depending on the CPL handedness and spin polarization of each layer. With the above results, we calculate the relative energy difference between the \mathcal{N}_0 and $-\mathcal{N}_0$ states under $\sigma\pm$ [Fig. 2(d)]. When the photon energy is below E_g , even though the χ' would reduce the energy potential [Eq. (2)], their energy difference remains to be zero as no light attenuation occurs. Above E_g , this model shows that $\sigma+$ ($\sigma-$) CPL favors $-\mathcal{N}_0$ (\mathcal{N}_0), under the synergistic effect of alternative light scattering and absorption over layers. Note that if the attenuation is ignored (setting $\lambda = 1$), the two states always keep their energetic degeneracy. Similarly, without including the scattering process, their degeneracy also retains if only absorption exists.

We vary the total layer number to conduct the calculation. From Fig. S3 [44], one sees that the bandgap of *A*-type AFM does not change significantly with respect to different layer numbers N . In addition, the sign and profile of $\Delta\mathcal{G}^{\sigma\pm}(\omega)$ remain to be independent of N . Interestingly, if N is increased, to obtain the same value of $\Delta\mathcal{G}^{\sigma\pm}$, the laser intensity can be linearly reduced. This is due to stronger light scattering and absorption occur for larger N system. Hence, in order to observe Néel vector flipping, one could conduct experimental measurement for relatively thicker multilayer systems. The thickness has to be constrained on the order of a few to a few tens of nanometers, below the light wavelength and penetration depth.

Realistic materials. We apply first-principle DFT calculations to adopt our theory into realistic materials, namely, MnBi_2Te_4 and CrI_3 . To reduce computational demands, we take bilayer systems here, which would give qualitatively the same results for thicker systems. The computational details can be found in SM [44]. As the conventional PBE functional [47, 48] underestimates the bandgap values, we adopt hybrid functional HSE06 [51, 52] corrections here. The atomic structure of MnBi_2Te_4 and its \mathcal{N}_0 configuration is plotted in Fig. 3(a). Our HSE06 calculated bandgap is $E_g = 0.454$ eV, consistent with previous results [57, 58]. In the bilayer model, the energy difference can be expressed in a compact way

$$\begin{aligned} \Delta\mathcal{G}^{\sigma\pm}(\omega) &= \mathcal{G}_{-\mathcal{N}_0}^{\sigma\pm}(\omega) - \mathcal{G}_{\mathcal{N}_0}^{\sigma\pm}(\omega) \\ &= \frac{d}{4c} I \left[\chi_{-\mathcal{N}_0}^{\sigma\pm'}(\mathbf{L}_2, \omega) A_{-\mathcal{N}_0}^{\sigma\pm}(\mathbf{L}_1, \omega) \right. \\ &\quad \left. - \chi_{\mathcal{N}_0}^{\sigma\pm'}(\mathbf{L}_2, \omega) A_{\mathcal{N}_0}^{\sigma\pm}(\mathbf{L}_1, \omega) \right]. \end{aligned} \quad (8)$$

Under \mathcal{C}_{3z} and $\mathcal{C}_{2x}\mathcal{T}$, this can be furthermore simplified into competing between diagonal and nondiagonal multiplications of susceptibility and absorbance between the two layers (see Supplemental Material [44]).

The layer-resolved optical responses are shown in Fig. S4 [44]. Our DFT results are well-converged and in fully

agreement with previously mentioned symmetry constraints. The top layer (\mathbf{L}_1) absorbs light on the order of $<\sim 5\%$, giving that attenuating factor $\lambda >\sim 95\%$. This would not generate enough heat in such a direct bandgap semiconductor, as most excited electron-hole pairs would recombine through direct radiative approaches. Hence, we ignore the thermal effect, which is in line with experimental observations [59]. As seen in Eq. (8), it is essential to lift the energy degeneracy between \mathcal{N}_0 and $-\mathcal{N}_0$ with nonzero attenuation. We then depict the energy difference between \mathcal{N}_0 and $-\mathcal{N}_0$, under $\sigma+$ and $\sigma-$ light [Figs. 3(b) and 3(c)]. Similar as in the model calculation, when the photon energy $\hbar\omega$ is below E_g , the two configurations are always degenerate, even though light scattering exists. When the light intensity I reaches 5×10^{11} W/cm² (corresponding to an electric field magnitude of $E_\omega = 0.14$ V/Å), the energy difference increases to be 0.06 meV/Å², which is about twice that of the magnetocrystalline anisotropy energy in bilayer MnBi_2Te_4 (calculated to be 0.03 meV/Å², consistent with previous works [34]). Such a light intensity can be achieved in the pulse form experimentally. For thicker multilayers, such an intensity can be furthermore reduced. One also note that once the Néel vector flips, it would not reverse back, indicating a non-volatile phase transition.

It is interesting to note that incident light frequency (or wavelength) could change the Néel direction preference. According to our calculations, when the photon energy $\hbar\omega$ is below 1.9 eV (corresponding to wavelength > 650 nm), $\sigma+$ light could induce the \mathcal{N}_0 state, while $\sigma-$ light gives the opposite $-\mathcal{N}_0$ configuration. If one increases the photon energy, the ground state reverses. At shorter wavelength (< 650 nm), $\sigma+$ irradiation would yield $-\mathcal{N}_0$ and $\sigma-$ drives the \mathcal{N}_0 to be more stable. We briefly compare our results with a recent experimental work [59], in which Qiu *et al.* have shown that $\sigma+$ light with wavelength shorter than $\sim 600 - 700$ nm could result in the negative Néel vector state (probed by magnetic circular dichroism). At longer wavelength, the preferred Néel vector reverses to be upward. If the light handedness is changed, the Néel vector direction also varies. This clearly demonstrates that the photo-magnetic interactions dominate during such a process, while thermal effect can be eliminated. Note that the light handedness and transition frequency as predicted in our theory is fully consistent with these experimental facts. Our numerical calculations are free of any experimental or experienced parameters, suggesting the validity of this microscopic mechanism.

As this nonreciprocal light scattering theory is not limited in axion insulators, we then use another *A*-type AFM, bilayer CrI_3 , to illustrate our theory. This material has been demonstrated theoretically and experimentally to possess an out-of-plane *A*-type AFM configuration. Our HSE06 calculation gives $E_g = 1.39$ eV.

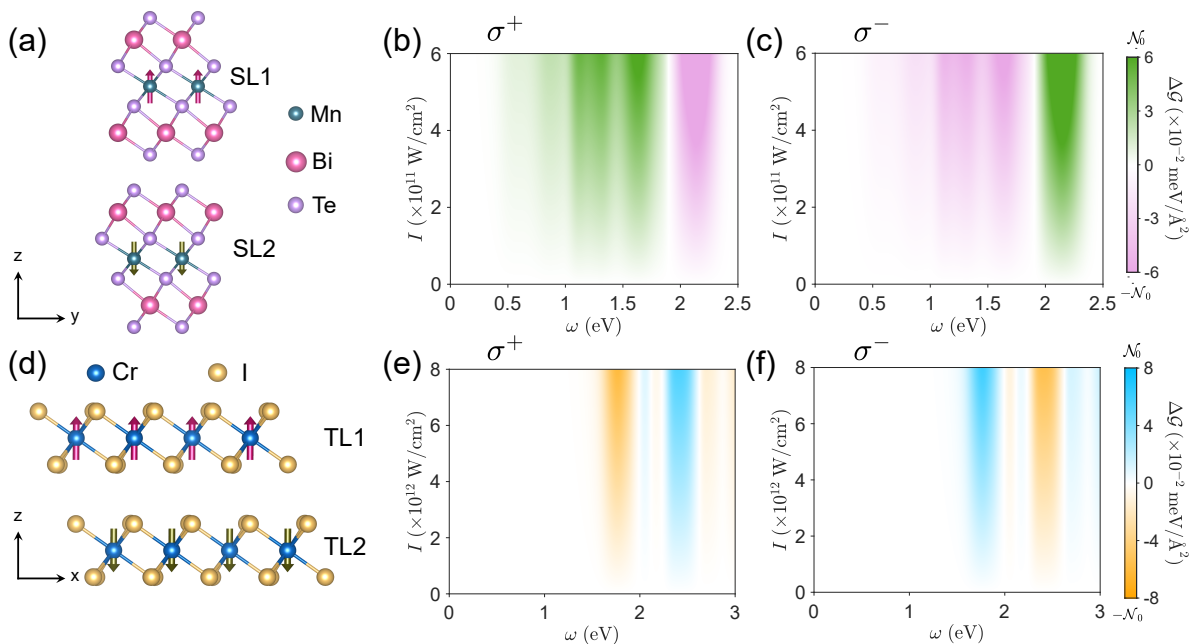


FIG. 3. DFT results on realistic materials. Atomic geometry of (a) MnBi_2Te_4 bilayer, and the phase diagram under (b) σ^+ and (c) σ^- light as functions of incident photon energy and light intensity. The light pulse duration is assumed to be 0.1 ps. The color scheme represents free energy difference, with pink and green indicate $-\mathcal{N}_0$ and \mathcal{N}_0 is preferable under light. (d)-(f) The results for CrI_3 bilayer under σ^+ and σ^- light irradiation. The \mathcal{N}_0 configuration is plotted in (a) and (d). SL and TL stand for atomic septuple layer and trilayer, respectively.

Hence, when $\hbar\omega \leq E_g$, the two Néel vectors remain to be degenerate. As the E_g is larger, light response functions in CrI_3 are in general smaller than MnBi_2Te_4 . Hence, the light intensity required for flipping Néel vector is larger. Above the E_g , light attenuation arises, but the layer-resolved absorbance remains to be within 1%, with a large λ value (Fig. S5 [44]). Above the bandgap, we see that σ^+ light favors $-\mathcal{N}_0$, which can be converted to \mathcal{N}_0 under σ^- light irradiation. The energy difference could reach $0.08 \text{ meV}/\text{\AA}^2$ under light of $I = 8 \times 10^{12} \text{ W}/\text{cm}^2$ ($E_\omega = 0.55 \text{ V}/\text{\AA}$), which is twice of the magnetocrystalline anisotropy energy (calculated to be $0.04 \text{ meV}/\text{\AA}^2$). Further increasing the photon energy to above a critical photon energy $\hbar\omega_{c1} \approx 2.1 \text{ eV}$ (wavelength of 590 nm) reverses the light handedness and its preferred Néel vector, namely σ^+ (σ^-) gives \mathcal{N}_0 ($-\mathcal{N}_0$). Such a trend flips again near a second critical photon energy $\hbar\omega_{c2} = 2.6 \text{ eV}$. At higher $\hbar\omega$, $\Delta\mathcal{G}^{\sigma^\pm}$ becomes smaller in magnitude, ascribed by the weaker nonreciprocal light scattering. Hence, we propose to use light with wavelength in between 500 – 830 nm to control Néel vector direction in AFM- CrI_3 .

Discussion. The simultaneous breaking of \mathcal{P} and \mathcal{T} here leads to optical diode effect, in analogous to semiconducting diode, and yields the nonreciprocal directional dichroism (NDD). Hence, this is another NDD mechanism in addition to the optical magnetoelectric (OME) coupling [27, 60, 61]. In general, the OME could occur

with low photon frequency, even at static limit, known as magnetoelectric responses and closely related to toroidal moment \mathbf{T} [62, 63]. We also note that layer-dependent susceptibility have been demonstrated to exhibit promising chiral and NDD magnetoelectric responses [64–66]. Our mechanism does not require the axion field to switch the Néel vector, and hence its material platform is not limited by axion insulators. We would like to remark that for the C -type or G -type AFMs, light incident direction may be switched to [110] or [111] directions, depending on how parallel spin planes are aligned. This is beyond the scope of current work, and will be discussed elsewhere.

Conclusion. In summary, we propose a nonreciprocal scattering mechanism to lift the energy degeneracy between Néel up and down configurations in \mathcal{PT} -AFMs under CPL illumination. We show that the light scattering effect (akin to the optical tweezer or ponderomotive potential) that has been largely overlooked could tilt the degeneracy of bistable Néel polarization. This is not limited to axion insulators that require strong diagonal magnetoelectric coupling coefficient. We illustrate our theory using a minimum $\mathbf{k} \cdot \mathbf{p}$ model, and *ab initio* DFT calculations in two realistic materials, giving consistent results as observed in very recent experiments. Our theory provides an alternative route to boosting optical diode effect.

The authors acknowledge valuable discussions with Yang Gao, Wenbin Li, Yandong Ma, Chengwang Niu, Hua Wang, Chunmei Zhang, and Hong Jian Zhao. This

work is supported by the National Natural Science Foundation of China (NSFC) under Grant No. 12374065. The Hefei Advanced Computing Center is acknowledged where the calculations are performed.

* jianzhou@xjtu.edu.cn

- [1] C. Kittel, “Theory of antiferroelectric crystals,” *Phys. Rev.* **82**, 729–732 (1951).
- [2] F. Keffer and C. Kittel, “Theory of antiferromagnetic resonance,” *Phys. Rev.* **85**, 329–337 (1952).
- [3] T. Jungwirth, X. Marti, P. Wadley, and J. Wunderlich, “Antiferromagnetic spintronics,” *Nat. Nanotech.* **11**, 231 (2016).
- [4] V. Baltz, A. Manchon, M. Tsoi, T. Moriyama, T. Ono, and Y. Tserkovnyak, “Antiferromagnetic spintronics,” *Rev. Mod. Phys.* **90**, 015005 (2018).
- [5] L. Šmejkal, Y. Mokrousov, B. Yan, and A. H. MacDonald, “Topological antiferromagnetic spintronics,” *Nat. Phys.* **14**, 242 (2018).
- [6] J. Han, R. Cheng, L. Liu, H. Ohno, and S. Fukami, “Coherent antiferromagnetic spintronics,” *Nat. Mater.* **22**, 684 (2023).
- [7] H. Chen, Q. Niu, and A. H. MacDonald, “Anomalous hall effect arising from noncollinear antiferromagnetism,” *Phys. Rev. Lett.* **112**, 017205 (2014).
- [8] S. Nakatsuji, N. Kiyohara, and T. Higo, “Large anomalous hall effect in a non-collinear antiferromagnet at room temperature,” *Nature* **527**, 212 (2015).
- [9] H. Kotegawa, H. Tanaka, Y. Takeuchi, H. Tou, H. Sugawara, J. Hayashi, and K. Takeda, “Large anomalous hall conductivity derived from an f -electron collinear antiferromagnetic structure,” *Phys. Rev. Lett.* **133**, 106301 (2024).
- [10] X. Yang, W. Feng, X. Zhou, Y. Mokrousov, and Y. Yao, “Intrinsic and extrinsic anomalous transport properties in noncollinear antiferromagnetic Mn_3Sn from first-principles calculations,” *Phys. Rev. B* **109**, 214406 (2024).
- [11] A. Gao, Y.-F. Liu, J.-X. Qiu, B. Ghosh, T. V. Trevisan, Y. Onishi, C. Hu, T. Qian, H.-J. Tien, S.-W. Chen, *et al.*, “Quantum metric nonlinear hall effect in a topological antiferromagnetic heterostructure,” *Science* **381**, 181–186 (2023).
- [12] C. Wang, Y. Gao, and D. Xiao, “Intrinsic nonlinear hall effect in antiferromagnetic tetragonal CuMnAs ,” *Phys. Rev. Lett.* **127**, 277201 (2021).
- [13] J. Wang, H. Zeng, W. Duan, and H. Huang, “Intrinsic nonlinear hall detection of the néel vector for two-dimensional antiferromagnetic spintronics,” *Phys. Rev. Lett.* **131**, 056401 (2023).
- [14] R. Mei, D. Kaplan, B. Yan, C.-Z. Chang, and C.-X. Liu, “Electrical control of intrinsic nonlinear hall effect in antiferromagnetic topological insulator sandwiches,” *Phys. Rev. B* **110**, 165401 (2024).
- [15] H. Wang and X. Qian, “Electrically and magnetically switchable nonlinear photocurrent in \mathcal{PT} -symmetric magnetic topological quantum materials,” *npj Comput. Mater.* **6**, 199 (2020).
- [16] Y. Zhang, T. Holder, H. Ishizuka, F. de Juan, N. Nagaosa, C. Felser, and B. Yan, “Switchable magnetic bulk photovoltaic effect in the two-dimensional magnet CrI_3 ,” *Nat. Commun.* **10**, 3783 (2019).
- [17] R. Fei, W. Song, and L. Yang, “Giant photogalvanic effect and second-harmonic generation in magnetic axion insulators,” *Phys. Rev. B* **102**, 035440 (2020).
- [18] C. Zhang, P. Guo, and J. Zhou, “Tailoring bulk photovoltaic effects in magnetic sliding ferroelectric materials,” *Nano Lett.* **22**, 9297–9305 (2022).
- [19] H. Pi, S. Zhang, and H. Weng, “Magnetic bulk photovoltaic effect as a probe of magnetic structures of EuSn_2As_2 ,” *Quantum Front.* **2**, 6 (2023).
- [20] D. Wu, M. Ye, H. Chen, Y. Xu, and W. Duan, “Giant and controllable nonlinear magneto-optical effects in two-dimensional magnets,” *npj Comput. Mater.* **10**, 79 (2024).
- [21] X. Li, T. Cao, Q. Niu, J. Shi, and J. Feng, “Coupling the valley degree of freedom to antiferromagnetic order,” *Proc. Natl. Acad. Sci. U.S.A.* **110**, 3738–3742 (2013).
- [22] Q. Xue, X. Mu, Y. Sun, and J. Zhou, “Valley contrasting bulk photovoltaic effect in a \mathcal{PT} -symmetric MnPS_3 monolayer,” *Phys. Rev. B* **107**, 245404 (2023).
- [23] L. Han, X. Fu, R. Peng, X. Cheng, J. Dai, L. Liu, Y. Li, Y. Zhang, W. Zhu, H. Bai, *et al.*, “Electrical 180° switching of néel vector in spin-splitting antiferromagnet,” *Sci. Adv.* **10**, eadn0479 (2024).
- [24] S. Yu. Bodnar, L. Šmejkal, I. Turek, T. Jungwirth, O. Gomonay, J. Sinova, A. A. Sapozhnik, H.-J. Elmers, M. Kläui, and M. Jourdan, “Writing and reading antiferromagnetic Mn_2Au by néel spin-orbit torques and large anisotropic magnetoresistance,” *Nat. Commun.* **9**, 348 (2018).
- [25] S. Reimers, Y. Lytvynenko, Y. R. Niu, E. Golias, B. Sarpi, L. S. I. Veiga, T. Denneulin, A. Kovács, R. E. Dunin-Borkowski, J. Blässer, *et al.*, “Current-driven writing process in antiferromagnetic Mn_2Au for memory applications,” *Nat. Commun.* **14**, 1861 (2023).
- [26] J. Godinho, H. Reichlová, D. Kriegner, V. Novák, K. Olejník, Z. Kašpar, Z. Šobán, P. Wadley, R. P. Campion, R. M. Otxoa, *et al.*, “Electrically induced and detected néel vector reversal in a collinear antiferromagnet,” *Nat. Commun.* **9**, 4686 (2018).
- [27] V. Kocsis, K. Penc, T. Röm, U. Nagel, J. Vít, J. Romhányi, Y. Tokunaga, Y. Taguchi, Y. Tokura, I. Kézsmárki, and S. Bordács, “Identification of antiferromagnetic domains via the optical magnetoelectric effect,” *Phys. Rev. Lett.* **121**, 057601 (2018).
- [28] G. P. Zhang and W. Hübner, “Laser-induced ultrafast demagnetization in ferromagnetic metals,” *Phys. Rev. Lett.* **85**, 3025–3028 (2000).
- [29] J. Chovan, E. G. Kavousanaki, and I. E. Perakis, “Ultrafast light-induced magnetization dynamics of ferromagnetic semiconductors,” *Phys. Rev. Lett.* **96**, 057402 (2006).
- [30] A. B. Henriques, X. Gratens, P. A. Usachev, V. A. Chitta, and G. Springholz, “Ultrafast light switching of ferromagnetism in EuSe ,” *Phys. Rev. Lett.* **120**, 217203 (2018).
- [31] N. Wu, S. Zhang, D. Chen, Y. Wang, and S. Meng, “Three-stage ultrafast demagnetization dynamics in a monolayer ferromagnet,” *Nat. Commun.* **15**, 2804 (2024).
- [32] Y. Deng, Y. Yu, M. Z. Shi, Z. Guo, Z. Xu, J. Wang, X. H. Chen, and Y. Zhang, “Quantum anomalous hall effect in intrinsic magnetic topological insulator MnBi_2Te_4 ,” *Science* **367**, 895–900 (2020).

- [33] D. Zhang, M. Shi, T. Zhu, D. Xing, H. Zhang, and J. Wang, “Topological axion states in the magnetic insulator mnbi_2te_4 with the quantized magnetoelectric effect,” *Phys. Rev. Lett.* **122**, 206401 (2019).
- [34] M. M. Otrokov, I. P. Rusinov, M. Blanco-Rey, M. Hoffmann, A. Yu. Vyazovskaya, S. V. Eremeev, A. Ernst, P. M. Echenique, A. Arnau, and E. V. Chulkov, “Unique thickness-dependent properties of the van der waals interlayer antiferromagnet mnbi_2te_4 films,” *Phys. Rev. Lett.* **122**, 107202 (2019).
- [35] B. Huang, G. Clark, E. Navarro-Moratalla, D. R. Klein, R. Cheng, K. L. Seyler, D. Zhong, E. Schmidgall, M. A. McGuire, D. H. Cobden, *et al.*, “Layer-dependent ferromagnetism in a van der waals crystal down to the monolayer limit,” *Nature* **546**, 270 (2017).
- [36] P. Zhang, T.-F. Chung, Q. Li, S. Wang, Q. Wang, W. L. B. Huey, S. Yang, J. E. Goldberger, J. Yao, and X. Zhang, “All-optical switching of magnetization in atomically thin cris_3 ,” *Nat. Mater.* **21**, 1373 (2022).
- [37] A. Kirilyuk, A. V. Kimel, and T. Rasing, “Ultrafast optical manipulation of magnetic order,” *Rev. Mod. Phys.* **82**, 2731–2784 (2010).
- [38] G. Pesce, “Optical tweezers: Theory and practice,” in *Encyclopedia of Condensed Matter Physics (Second Edition)*, edited by T. Chakraborty (Academic Press, Oxford, 2024) second edition ed., pp. 317–333.
- [39] J. Zhou, H. Xu, Y. Shi, and J. Li, “Terahertz driven reversible topological phase transition of monolayer transition metal dichalcogenides,” *Adv. Sci.* **8**, 2003832 (2021).
- [40] Z. Wu, K. Liu, X. Mu, and J. Zhou, “Renormalizing antiferroelectric nanostripes in β' - In_2Se_3 via optomechanics,” *J. Phys. Chem. Lett.* **14**, 677–684 (2023), pMID: 36637877.
- [41] J. Shi, Y.-Q. Bie, A. Zong, S. Fang, W. Chen, J. Han, Z. Cao, Y. Zhang, T. Taniguchi, K. Watanabe, *et al.*, “Intrinsic $1\text{t}'$ phase induced in atomically thin 2h-mote_2 by a single terahertz pulse,” *Nat. Commun.* **14**, 9505 (2023).
- [42] J. Shi, C. Heide, H. Xu, Y. Huang, Y. Shen, B. Guzelturk, M. Henstridge, C. F. Schön, A. Mangu, Y. Kobayashi, *et al.*, “Nonresonant raman control of material phases,” (2024), [arXiv:2411.10131](https://arxiv.org/abs/2411.10131) [physics.optics].
- [43] Z. Sun, “Floquet engineering of many-body states by the ponderomotive potential,” *Phys. Rev. B* **110**, 104301 (2024).
- [44] See Supplemental Material at URL-will-be-inserted-by-publisher for the discussions on continuum model, $k \cdot p$ model results, and details on first-principles DFT calculations that include references.
- [45] G. Kresse and J. Hafner, “Ab initio molecular dynamics for liquid metals,” *Phys. Rev. B* **47**, 558–561 (1993).
- [46] G. Kresse and J. Furthmüller, “Efficient iterative schemes for ab initio total-energy calculations using a plane-wave basis set,” *Phys. Rev. B* **54**, 11169–11186 (1996).
- [47] J. P. Perdew, K. Burke, and M. Ernzerhof, “Generalized gradient approximation made simple,” *Phys. Rev. Lett.* **77**, 3865–3868 (1996).
- [48] J. P. Perdew, A. Ruzsinszky, G. I. Csonka, O. A. Vydrov, G. E. Scuseria, L. A. Constantin, X. Zhou, and K. Burke, “Restoring the density-gradient expansion for exchange in solids and surfaces,” *Phys. Rev. Lett.* **100**, 136406 (2008).
- [49] P. E. Blöchl, “Projector augmented-wave method,” *Phys. Rev. B* **50**, 17953–17979 (1994).
- [50] H. J. Monkhorst and J. D. Pack, “Special points for brillouin-zone integrations,” *Phys. Rev. B* **13**, 5188–5192 (1976).
- [51] J. Heyd, G. E. Scuseria, and M. Ernzerhof, “Hybrid functionals based on a screened coulomb potential,” *J. Chem. Phys.* **118**, 8207–8215 (2003).
- [52] J. Heyd, G. E. Scuseria, and M. Ernzerhof, “Erratum: Hybrid functionals based on a screened coulomb potential [j. chem. phys. 118, 8207 (2003)],” *J. Chem. Phys.* **124**, 219906 (2006).
- [53] A. A. Mostofi, J. R. Yates, G. Pizzi, Y.-S. Lee, I. Souza, D. Vanderbilt, and N. Marzari, “An updated version of wannier90: A tool for obtaining maximally-localised wannier functions,” *Comput. Phys. Commun.* **185**, 2309–2310 (2014).
- [54] C. Lei, S. Chen, and A. H. MacDonald, “Magnetized topological insulator multilayers,” *Proc. Natl. Acad. Sci. U.S.A.* **117**, 27224–27230 (2020).
- [55] A. A. Burkov and L. Balents, “Weyl semimetal in a topological insulator multilayer,” *Phys. Rev. Lett.* **107**, 127205 (2011).
- [56] M. Gajdoš, K. Hummer, G. Kresse, J. Furthmüller, and F. Bechstedt, “Linear optical properties in the projector-augmented wave methodology,” *Phys. Rev. B* **73**, 045112 (2006).
- [57] F. Xue, Y. Hou, Z. Wang, Z. Xu, K. He, R. Wu, Y. Xu, and W. Duan, “Tunable quantum anomalous hall effects in ferromagnetic van der waals heterostructures,” *Natl. Sci. Rev.* **11**, nwad151 (2023).
- [58] C. X. Trang, Q. Li, Y. Yin, J. Hwang, G. Akhgar, I. Di Bernardo, A. Grubišić-Čabo, A. Tadich, M. S. Fuhrer, S.-K. Mo, *et al.*, “Crossover from 2d ferromagnetic insulator to wide band gap quantum anomalous hall insulator in ultrathin MnBi_2Te_4 ,” *ACS Nano* **15**, 13444–13452 (2021).
- [59] J.-X. Qiu, C. Tzschaschel, J. Ahn, A. Gao, H. Li, X.-Y. Zhang, B. Ghosh, C. Hu, Y.-X. Wang, Y.-F. Liu, *et al.*, “Axion optical induction of antiferromagnetic order,” *Nat. Mater.* **22**, 583 (2023).
- [60] T. Sato, N. Abe, S. Kimura, Y. Tokunaga, and T.-h. Arima, “Magnetochiral dichroism in a collinear antiferromagnet with no magnetization,” *Phys. Rev. Lett.* **124**, 217402 (2020).
- [61] K. Kimura, Y. Otake, and T. Kimura, “Visualizing rotation and reversal of the néel vector through antiferromagnetic trichroism,” *Nat. Commun.* **13**, 697 (2022).
- [62] C. Ederer and N. A. Spaldin, “Towards a microscopic theory of toroidal moments in bulk periodic crystals,” *Phys. Rev. B* **76**, 214404 (2007).
- [63] N. A. Spaldin, M. Fiebig, and M. Mostovoy, “The toroidal moment in condensed-matter physics and its relation to the magnetoelectric effect,” *J. Phys.: Condens. Matter* **20**, 434203 (2008).
- [64] T. Stauber, T. Low, and G. Gómez-Santos, “Chiral response of twisted bilayer graphene,” *Phys. Rev. Lett.* **120**, 046801 (2018).
- [65] Y. Gao, Y. Zhang, and D. Xiao, “Tunable layer circular photogalvanic effect in twisted bilayers,” *Phys. Rev. Lett.* **124**, 077401 (2020).
- [66] W. Liang, J. Zeng, Z. Qiao, Y. Gao, and Q. Niu, “Berry-curvature engineering for nonreciprocal directional dichroism in two-dimensional antiferromagnets,” *Phys. Rev. Lett.* **131**, 256901 (2023).